

UC Berkeley

UC Berkeley Previously Published Works

Title

Temperature measurement of a turbulent buoyant ethylene diffusion flame using a dual-thermocouple technique

Permalink

<https://escholarship.org/uc/item/4t58r3p1>

Authors

Ren, Xingyu
Zeng, Dong
Wang, Yi
[et al.](#)

Publication Date

2021-03-01

DOI

10.1016/j.firesaf.2020.103061

Peer reviewed

1 **Temperature measurement of a turbulent buoyant ethylene diffusion flame using a dual-**
2 **thermocouple technique**

3 Xingyu Ren^a, Dong Zeng^{b*}, Yi Wang^b, Gang Xiong^b, Gaurav Agarwal^b, Michael Gollner^{a,c*}

4 ^aDepartment of Fire Protection Engineering, University of Maryland, College Park, MD, USA,

5 ^bResearch Division, FM Global, 1151 Boston-Providence Turnpike, Norwood, MA 02062, USA,
6 dong.zeng@fmglobal.com

7 ^cDepartment of Mechanical Engineering, University of California, Berkeley, CA, USA

8 *mgollner@berkeley.edu

9 **Highlights:**

- 10 • A temperature dataset is established for a buoyant turbulent ethylene flame.
11 • A dual-thermocouple technique is used to compensate turbulent gas temperatures.
12 • Mean, root-mean square and probability density function temperatures are provided.

13

14 **Abstract:**

15 High-frequency temperature measurements were carefully conducted for a 15 kW buoyant
16 turbulent ethylene diffusion flame over a 15.2 cm diameter gas burner with air co-flow. A dual-
17 thermocouple probe, consisting of two fine-wire thermocouples with 25 μm and 50 μm wire
18 diameters, was used to determine a compensated turbulent gas temperature. A sensitivity analysis
19 shows that temperatures resolved using this dual-thermocouple technique are less sensitive to
20 changes in thermocouple bead size, therefore, uncertainty is greatly reduced even when soot
21 deposition on the thermocouple bead occurs in sooty flames. Mean and root-mean square (rms)
22 fluctuations of gas temperature were recorded in a two-dimensional plane across the flame
23 centerline. The mean gas temperature monotonically decreases away from the flame centerline at
24 most flame heights, except for 1 diameter above the burner, where a temperature dip is observed.
25 The rms temperature peaks shift from the edge of the flame to the center as the height increases.
26 This is due to the enhanced mixing between fuel and air, which is further shown using
27 probability density functions of the local gas temperature. A systematic temperature dataset with
28 high spatial resolution is established for sooty flames, which is valuable for future soot and
29 radiation model validation.

30

31 **Keywords:** local gas temperature; dual-thermocouple technique; time constant; probability
32 density function; validation dataset

33

34 **1. Introduction**

35 Fire modeling has become a critical tool in fire science, used in both research and applied design
36 scenarios. Two large-eddy simulation (LES)-based models in particular are commonly used in
37 the field, FireFOAM [1,2] and the Fire Dynamics Simulator (FDS) [3]. Fundamental physical
38 and chemical models are integrated into these computational codes to capture multi-physics,
39 multi-scale fire dynamics including a combination of chemical reactions, turbulent mixing,
40 thermal and fluid dynamics. In order to use these models for research or applied scenarios,
41 validation must occur both for realistic scenarios and of underlying physical models used in
42 simulations. In order to perform such validations, high accuracy experimental datasets are
43 needed.

44 The gas-phase temperature serves as an important fire characteristic, as it provides a direct scalar
45 comparison with computational results. However, the turbulent reactive flow field in fires makes
46 it challenging to obtain time-resolved temperature information. To date, researchers have used
47 thermocouples, thin-filament pyrometry, multi-color optical probes and coherent anti-Stokes
48 Raman scattering (CARS) thermometry to measure local gas temperatures in various
49 configurations. CARS [4] appears to be the most unobtrusive way to measure local gas
50 temperature without modifying the flame; however, the complex experimental setup requires an
51 extensive investment and considerable calibration. Thin-filament pyrometry has also been
52 successfully applied on both a methanol pool fire and a blue whirl [5–7]; however, this technique
53 is limited to soot-free flames which don't reflect most practical scenarios. Multi-color optical
54 probes feature simultaneous soot volume fraction and temperature measurements, however only
55 soot, not gas temperature can be detected [8]. Thermocouples, on the other hand, have been
56 widely used for high temperature measurements [9–11]; however, physical and mathematical
57 models need to be employed to account for the thermal inertia of the thermocouple bead under
58 turbulent, fluctuating fire conditions.

59 Several methods have been proposed to compensate for the thermal inertial effect and
60 reconstruct the true local temperature from raw thermocouple readings [12–21]. The frequency
61 response of a thermocouple, in principle, is a first-order lag system and can be compensated for
62 using a first-order coefficient, namely a time constant. For a steady combustion process, the
63 mean time constant of a thermocouple bead can be determined using an electrical heating method
64 [15]. However, the dramatic fluctuations in both temperature and velocity in a fire environment
65 leads to a varying time constant, where use of a mean value might lead to both over- and under-
66 compensation of temperature signals. Measurement of the instantaneous time constant in
67 turbulent conditions can be extremely difficult as it is a function of the local temperature and
68 velocity, requiring synchronized measurements [16]. Previously, a dual-thermocouple technique
69 has been proposed to estimate the fluctuating time constant without direct measurement of
70 velocity [17–19]. This technique relies on assumption of fixed bead sizes of the thermocouples,
71 which may change in sooty environments, ultimately introducing large errors [17]. Further
72 improvements of the dual-thermocouple technique show a possible application in sooty flames,
73 as the instantaneous time constant can be estimated without assuming bead diameters, only
74 incorporating diameters to compensate for radiant losses [20,21].

75 In this work, local gas temperature measurements of buoyant, turbulent, ethylene diffusion
76 flames have been conducted using a dual-thermocouple (dual-TC) probe made with two type-S
77 fine-wire thermocouples. In alignment with the IAFSS Working Group on Measurement and
78 Computation of Fire Phenomena (i.e. the MaCFP Working Group) [22,23], the present work
79 aims to provide a detailed temperature validation dataset for a MaCFP target test case. Medium-
80 scale, 15 kW ethylene diffusion flames are produced using a 15.2 cm round water-cooled burner
81 with a controlled co-flow at FM Global's laboratory [8]. This test case is intended to provide a
82 dataset to validate soot and radiation models in buoyant flames. The radiative characteristics,
83 including radiant power distribution, local soot volume fraction and soot temperature under
84 normal and reduced-oxygen conditions have been reported in [8]. Here, temperature
85 measurements including local mean, root-mean square (rms) fluctuation, and probability
86 distribution profiles are presented, which are necessary for future development of this validation
87 dataset.

88

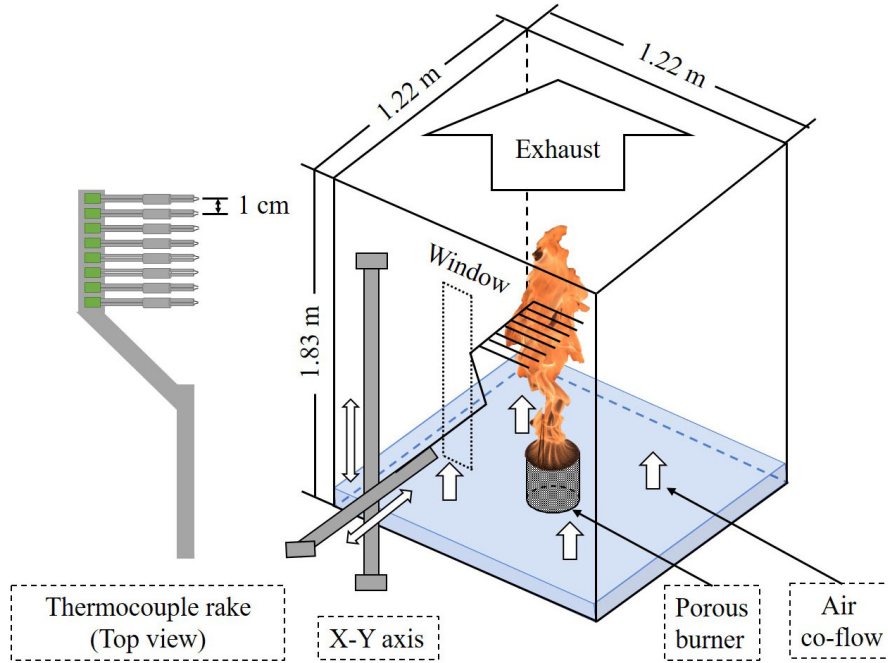
89 2. Experimental setup

90 A 15 kW buoyancy-driven turbulent diffusion flame is produced in a 1.22 by 1.22 m² wide, 1.83
91 m tall water-cooled enclosure [8], as shown in Fig. 1. Chemically pure ethylene (>99.9%) was
92 fed through a mass flow controller to a 15.2 cm diameter round gas burner. Before reaching the
93 burner surface, fuel passes through a honeycomb with a 0.32 cm cell size and 2 cm thickness
94 followed by two layers of coarse and fine steel beads (with a 2.54 cm thick layer of 0.48 cm
95 diameter beads and a 2.54 cm thick layer of 0.31 cm diameter beads, respectively) to assure a
96 uniform exit flow velocity. Air co-flow is supplied through a rotameter with a mass flow rate of
97 52 g/s and an uncertainty of $\pm 10\%$. Uniform air co-flow was achieved after passing through a
98 plenum of fine screens and a 3.81 cm thick layer of sand. During each test, the water-cooled
99 burner surface remains at about 353 K. More details of this setup are reported in [8].

100 The dual-TC pair was made with two type-S thermocouples, with 25 μm and 50 μm wire
101 diameters (Omega Engineering, P10R-001 and P10R-002). The corresponding average bead
102 diameters are measured as 88 μm and 126 μm , respectively, using a microscope. The
103 thermocouple wires were supported by a single 1.6 mm diameter twin bore ceramic cylinder
104 (Omega Engineering, TRX-164116) with a smaller ~ 8 mm length of thermocouple wire exposed.
105 The beads of the dual-TC were positioned about 0.5 mm apart to ensure both thermocouples are
106 exposed to nearly identical thermal field conditions. The validity of the identical surrounding
107 condition assumption was tested using two identical thermocouples with 50 μm wire diameter. A
108 15 cm methanol pool fire was selected to minimize any affects caused by soot. The resultant
109 cross-correlation coefficient of the signal fluctuations, $R_{12} = \overline{T'_{th1} T'_{th2}} / (\overline{T'^2_{th1}} \overline{T'^2_{th2}})^{1/2}$, has a
110 value larger than 0.98, indicating that both thermocouples measure the same surrounding gas
111 temperature.

112 During tests, a thermocouple rake using 8 pairs of dual-TCs with a 1-cm interval was traversed
113 in a two-dimensional plane across the burner centerline by a stepper-motor driven X-Y axis with
114 10 μm accuracy. After putting in the thermocouple rake, the symmetry of the flame was ensured

115 using averaged flame images over 60 s (recorded at 30 fps). Observation of the flame through the
 116 testing window was made for each experiment, no significant changes were observed to be
 117 introduced by the thermocouple rake. For the vertical direction, measurements were taken from
 118 $1.0D$ (D is the burner diameter) to $3.5D$ with a $0.5D$ interval, for the radial direction,
 119 measurements were taken from 0 cm at the flame centerline to 11 cm away from the centerline,
 120 with 1 cm intervals. Temperature signals, in μV , were digitally sampled at 5 kHz for 60 s at each
 121 point. The voltage signals were converted to temperature using a NIST table [24] for type-S
 122 thermocouples. A cold junction correction was considered for all cases.



123
 124 Fig. 1. Schematic of the experimental setup

125
 126 **3. Thermocouple compensation methods**

127 Due to the thermal inertial of the thermocouple bead, high-frequency temperature fluctuations
 128 recorded by a micro thermocouple (typically with a wire diameter from $25\ \mu\text{m}$ to $125\ \mu\text{m}$) are
 129 attenuated. In order to reconstruct local gas temperature, a time constant is needed to compensate
 130 the measured temperature. Both single and dual-thermocouple methods are discussed below to
 131 calculate the time constant.

132
 133 **3.1 Single-thermocouple method**

134 A heat balance for a single thermocouple (Single-TC) bead under an unsteady turbulent flame
 135 with negligible conduction to lead wires can be written as

136
$$m c_p \frac{dT_{th}}{dt} = A [(T_g - T_{th}) * h - \varepsilon \sigma T_{th}^4 + \varepsilon \dot{q}''_{rad}], \quad (1)$$

137 where the left-hand side (LHS) of the equation represents the energy change of the thermocouple
 138 bead, m is the bead mass (kg), c_p is the bead heat capacity (J/kg · K), and T_{th} is the
 139 thermocouple bead temperature (K). The right-hand side (RHS) includes convective
 140 heating/cooling, radiant heat losses from the bead, and radiant heat absorption of bead from the
 141 surrounding fire, respectively. Heat absorption from the ambient air is sufficiently small and is
 142 ignored. Here, A is the bead area (m²), T_g is the local gas temperature (K), h is the heat-transfer
 143 coefficient (W/m²K), ε is the bead emissivity (assumed to be 0.95 for soot-coated bead), and
 144 \dot{q}''_{rad} is the radiant heat flux (W/m²) from the surrounding fire. Eq. 1 can be re-written with T_g
 145 on the LHS,

$$146 \quad T_g = T_{th} + \frac{V}{A} \frac{\rho c_p}{h} \frac{dT_{th}}{dt} + \frac{1}{h} (\varepsilon \sigma T_{th}^4 - \varepsilon \dot{q}''_{rad}) \quad (2)$$

147 where h can be calculated as $Nu k_g / d$, with Nu representing the Nusselt number, k_g being the
 148 temperature-dependent thermal conductivity (W/mK) of gas, and d being the thermocouple bead
 149 diameter (m). Further, V/A represents the inverse of a surface to volume ratio of a thermocouple
 150 bead and ρ is the bead density (kg/m³). According to observations of thermocouples used in this
 151 study using a microscope, a spherical structure is assumed for the thermocouple beads, providing
 152 $V/A = d/6$. In some previous studies a cylindrical structure is also used [13,20], resulting in
 153 $V/A = d/4$. Substituting the above parameters into Eq. 2 provides

$$154 \quad T_g = T_{th} + \frac{\rho c_p d^2}{6Nu k_g} \frac{dT_{th}}{dt} + \frac{d}{Nu k_g} (\varepsilon \sigma T_{th}^4 - \varepsilon \dot{q}''_{rad}), \quad (3)$$

155 where

$$156 \quad Nu = 2 + 0.6Re^{1/2}Pr^{0.4} \quad (4)$$

157 and

$$158 \quad \tau = \frac{\rho c_p d^2}{6Nu k_g}. \quad (5)$$

159 Using a Nu correlation for flow around a sphere [25] from Eq. 4, where Re is the Reynolds
 160 number (Ud/ν , where ν is the kinematic viscosity of the fluid in m²/s), and Pr is the Prandtl
 161 number (ν/α , where α is the thermal diffusivity of the fluid in m²/s), the time constant can be
 162 calculated using Eq. 5 [20,25], ultimately becoming a strong function of local gas velocity,
 163 temperature and bead diameter, i.e. $\tau = f(U, T_g, d)$. The local gas temperature in Eq. 3 can then
 164 be solved after accounting for any additional external \dot{q}''_{rad} .

165 In practice, the complex geometry of the thermocouple bead and wire combination leads to large
 166 uncertainties in bead diameter. Especially for sooty flames, soot deposits on the thermocouple
 167 bead due to thermophoresis and leads to growth of the bead size throughout the duration of
 168 measurements. To determine the influence of this phenomena on measured temperatures and
 169 response rates, a sensitivity and uncertainty study was conducted. A temperature signal sampled
 170 in the flame centerline at a height of $2.5D$ was used. Normalized sensitivity $s(T_{g,i})$ and absolute
 171 uncertainty values $u(T_{g,i})$ were calculated using following equations [26,27],

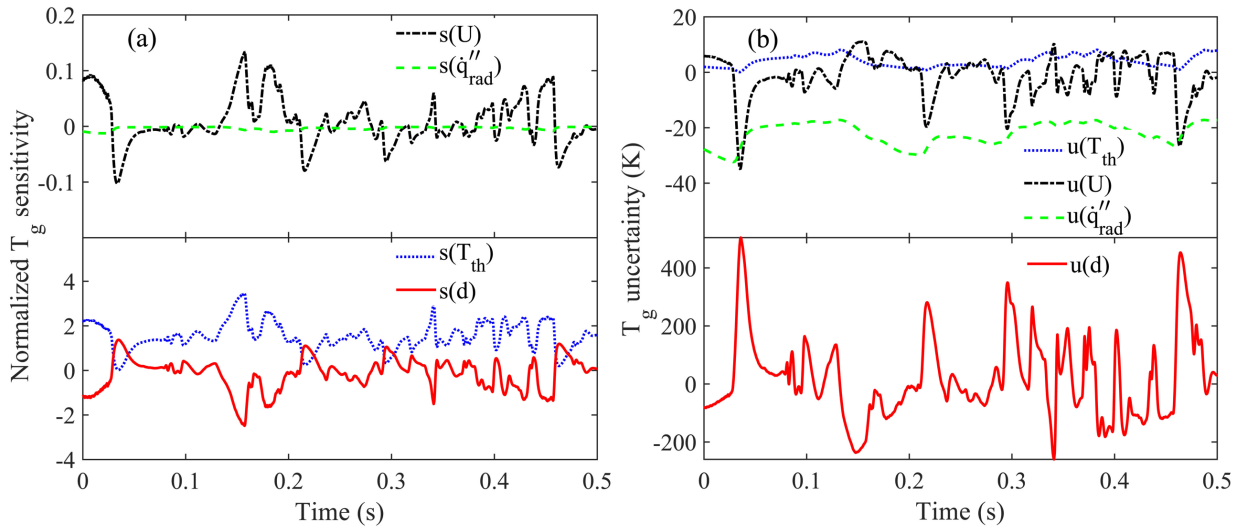
$$172 \quad s(T_{g,i}) = \frac{x_i}{T_{g,i}} \frac{\partial T_{g,i}}{\partial x_i} \quad (6)$$

173

$$u(T_{g,i}) = \Delta x_i \frac{\partial T_{g,i}}{\partial x_i}, \quad (7)$$

174 where x_i is the input variable at step i and Δx_i is the uncertainty of any input parameter x_i .

175 Fig. 2(a) shows the sensitivities of the time-resolved compensated T_g signal to the measured
 176 parameters. We can see T_g is very sensitive to the original thermocouple output temperature T_{th}
 177 and bead diameter d , and less sensitive to the local gas velocity U and radiant heat flux \dot{q}''_{rad} . In
 178 experiments, the relative uncertainty of T_{th} is relative small, estimated to be 0.25% for a type-S
 179 thermocouple and associated data acquisition system, thus the overall T_g uncertainty is ± 10 K
 180 within a 95% confidence interval (CI) in the flame, shown in Fig. 2(b). For velocity
 181 measurements, a 1.4 m/s flow velocity has been used based on previous measurement at FM
 182 Global using particle image velocimetry (PIV). A 20% measurement uncertainty is assigned in
 183 this analysis due to the fluctuating fire environment, with a resulting uncertainty of ± 14 K at
 184 95% CI. For a small thermocouple bead, the effect of radiant heat flux on the temperature
 185 correction can usually be ignored. In the present work, with a 15 kW ethylene flame
 186 approximately 0.7 m in height and 0.152 m in diameter, the radiant heat flux to a thermocouple
 187 bead at the flame centerline and a height of $2.5D$, may be as high as 45 kW/m², see Appendix
 188 A. This external radiant heat flux results in an uncertainty ranging from -28 K to -16 K in a
 189 95% CI for the 25 μ m diameter wire (88 μ m bead diameter). The bead diameter, on the other
 190 hand, is conservatively estimated to change only 20%, even though soot deposition may cause
 191 even more significant changes. The resulting uncertainty reaches -199 K to 297 K in a 95% CI.
 192 The preceding analysis demonstrates that the single-TC compensation method is most sensitive
 193 to thermocouple bead diameter, with inaccurate bead size measurements leading to large
 194 temperature uncertainty, which may be exacerbated in sooty flames.



195

196 Fig. 2. Time-resolved sensitivities (s) and uncertainties (u) of single-TC method: (a) Normalized
 197 T_g sensitivities, (b) Absolute T_g uncertainties.

198

199 3.2 Dual-thermocouple method

200 A dual-thermocouple (Dual-TC) method has been proposed by Tagawa and Oath [20] to
 201 compensate the local gas temperature which is less affected by the geometrical features of the
 202 thermocouple beads. The basic assumption is that, by putting two fine-wire thermocouple beads
 203 close together, typically less than 0.5 mm, both thermocouples are under identical surrounding
 204 conditions. The following two equations are then formed for two thermocouples,

$$205 \quad T_{g1} = T_{th1} + \tau_1 \left(\frac{dT_{th1}}{dt} - \frac{6}{\rho c_p} \left(\frac{\varepsilon \dot{q}_{rad}'' - \varepsilon \sigma T_{th1}^4}{d_1} \right) \right) \quad (8)$$

$$206 \quad T_{g2} = T_{th2} + \tau_2 \left(\frac{dT_{th2}}{dt} - \frac{6}{\rho c_p} \left(\frac{\varepsilon \dot{q}_{rad}'' - \varepsilon \sigma T_{th2}^4}{d_2} \right) \right), \quad (9)$$

207 where the subscripts 1 and 2 denote two thermocouples with diameters of d_1 (88 μm) and d_2
 208 (126 μm), respectively. Assuming identical surrounding conditions,

$$209 \quad T_{g1} = T_{g2} = T_g, \quad (10)$$

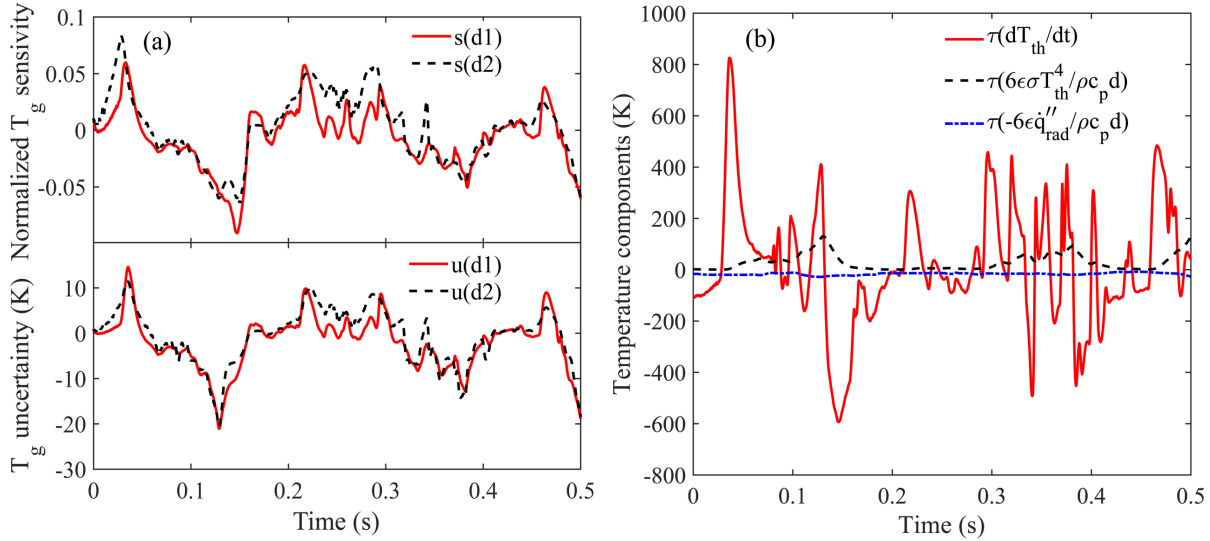
210 which implies that both compensated temperatures should equal the true local gas temperature.
 211 Equation 10 holds true for all temperature pairs; therefore, the problem is reduced to finding τ_1
 212 and τ_2 to satisfy Eq. 10 for temperature pairs measured at all times. Assuming there are a total of
 213 N pairs of measurements, Eq. 8 and Eq. 9 can be solved for by finding τ_1 and τ_2 to minimize Eq.
 214 11 using a least-squares method

$$215 \quad e = \frac{\sum_1^N |T_{g1} - T_{g2}|}{N}. \quad (11)$$

216 The duration over which N pairs of temperature signals are acquired is defined as the time
 217 window. In order to include sufficient data points to evaluate τ_1 and τ_2 , a time window needs to
 218 be selected that is large enough to reflect the heat transfer process but, ideally, small enough to
 219 resolve turbulent fluctuations. Selection of a time window that is too short may result in
 220 unrealistic time constants. Previous literature [20,21] suggest a time window selection between
 221 1.5 ~ 3.0 times of the mean time constant of the thinner thermocouple. In the present work, a
 222 0.06 s ($\sim 4\bar{\tau}_1$, where $\bar{\tau}_1$ is the mean time constant of the 25 μm wire thermocouple) time window
 223 was used. The mean time constant $\bar{\tau}_1$ was obtained through use of all temperature data points
 224 with a least squares method (i.e. a 60 s signal with a 5 kHz sampling rate, totaling 300,000 data
 225 points).

226 The advantage of this dual-TC scheme is that the thermocouple bead diameters are only used to
 227 calculate the radiant loss term, which results in less uncertainty. Measured velocities are no
 228 longer needed, which makes the experiments more convenient and cost effective. Sensitivity and
 229 uncertainty analyses were conducted to evaluate the effect of the bead diameter. Fig. 3(a) shows
 230 the sensitivities and uncertainties of the two thermocouple beads. Compared with the single-TC
 231 method, T_g is much less sensitive to the bead diameter. A 20% increase in diameter leads to only
 232 a - 25 K to 8 K uncertainty at a 95% CI, which is much less than the uncertainties induced by the
 233 single TC method. The temperature compensation contributed by different terms in Eq. 8 is
 234 plotted in Fig.3(b). As shown, the most important term is $\tau (dT_{th}/dt)$, which represents the
 235 contribution of convective heating, while the radiant heat loss term, $\tau(6\varepsilon\sigma T_{th}^4/\rho c_p d)$, plays a

236 secondary role. For the radiant absorption term, $\tau(-6\epsilon\dot{q}_{rad}''/\rho c_p d)$, a 45 kW/m² heat flux leads
 237 to a temperature compensation ranging from -31 K to -2 K in a 95% CI. Considering the
 238 uncertainties caused by a 0.25% data acquisition error, a 20% bead size change, and a
 239 45 kW/m² external radiant heat flux, the overall uncertainty on the compensated local hot gas
 240 temperature T_g was estimated at ± 41 K.



241
 242 Fig. 3. (a) Time-resolved sensitivities and uncertainties on thermocouple bead diameter of dual-
 243 TC methods, (b) Time-resolved temperature compensation components on a 25 μm wire
 244 diameter TC

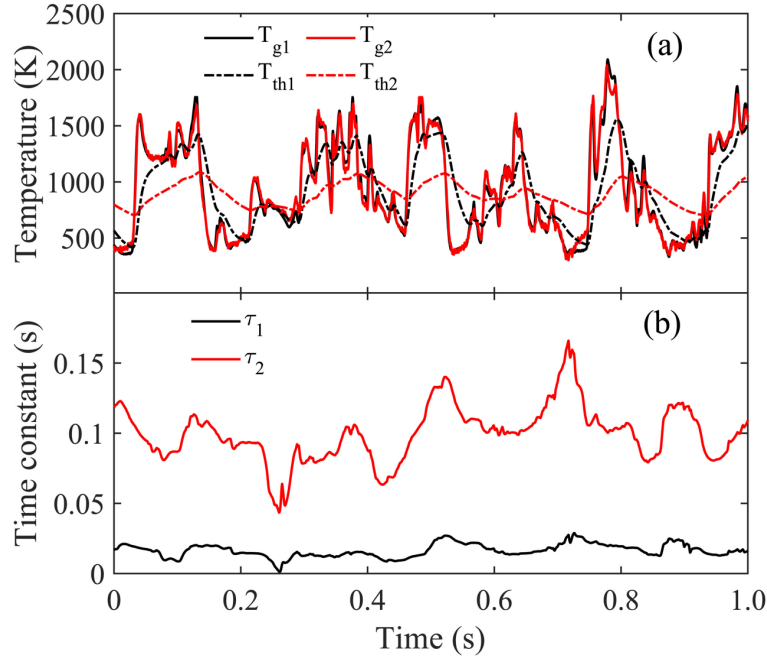
245
 246 **4. Results and discussion**

247 **4.1 Compensated temperature signal**

248 Fig. 4(a) shows an example of a 1 s duration of compensated temperatures and the corresponding
 249 fluctuating time constants along the flame centerline at a height of $2.5D$. Uncompensated
 250 temperatures from the 25 μm wire diameter TC, T_{th1} show a higher sensitivity and wider
 251 temperature range than the 50 μm wire diameter T_{th2} measurements due to its smaller thermal
 252 inertia. Although both T_{th1} and T_{th2} reflect fluctuations in the flow field, details, especially in
 253 higher and lower temperature ranges, are missing (T_{th1} : 400 ~ 1770 K, T_{th2} : 620 ~ 1280 K). In
 254 comparison, the compensated temperature signals T_{g1} and T_{g2} show good agreement, with a
 255 cross-correlation coefficient around 0.99. Compensated temperature fluctuations with a higher
 256 frequency resolution show a broader temperature range, from 300 K ~ 2100 K, where the lower
 257 and upper limits correspond to the ambient air temperature and flame temperature of ethylene,
 258 respectively. The maximum temperature in a turbulent ethylene diffusion flame should be less
 259 than the adiabatic flame temperature of ethylene, i.e. 2370 K, primarily due to radiant losses. A
 260 power spectral density analysis shows that the compensated temperature signal has a frequency
 261 up to 600 Hz, which is able to resolve a majority of the gas temperature fluctuations shown in
 262 Fig. 4(a).

263

264 The computed time constants are shown in Fig. 4(b). Both time constant signals fluctuate with
265 changes in the surrounding flow field and follow the same trend. The 25 μm wire thermocouple
266 has a smaller fluctuating time constant, with a mean value of 0.015 s, while for the larger wire
267 diameter the time constant is 6 to 7 times larger.



268

269 Fig. 4. Time resolved compensated temperature and time constants at the flame centerline and a
270 height of $2.5D$: (a) raw and compensated gas temperature, (b) calculated fluctuating time
271 constants.

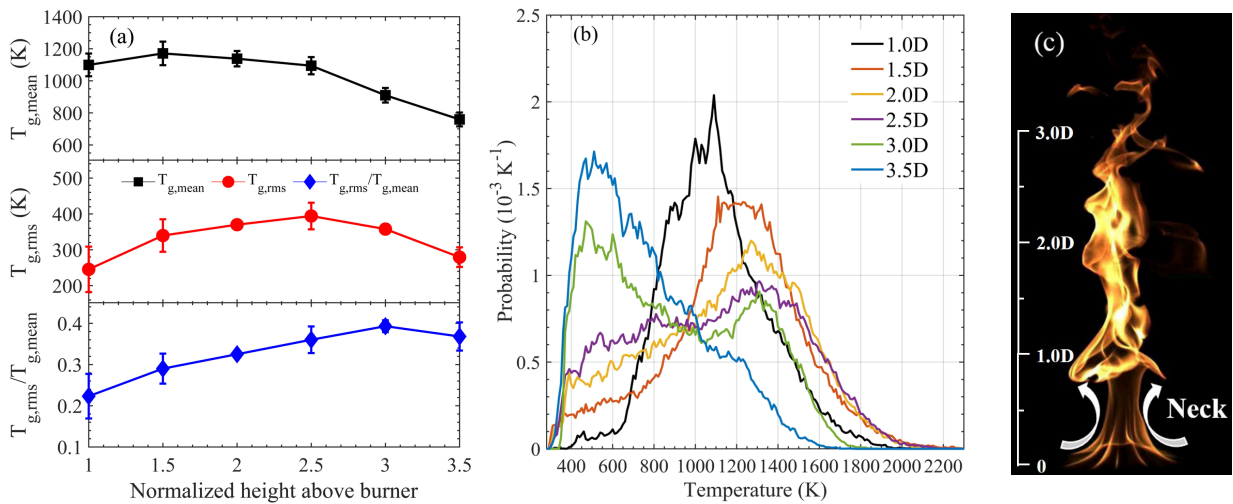
272 Auto-correlation of the temperature signals shows this flame has a Taylor-micro time scale
273 ranging from 0.02 to 0.04 s, from the centerline to the outer edge of the flame. Assuming a
274 1.4 m/s centerline vertical gas velocity at a height of $2.5D$ above the burner, as well as Taylor's
275 frozen turbulence hypothesis, the Taylor microscale at the flame centerline is calculated to be
276 ~ 0.028 m. Weckman [16] previously investigated the turbulent structures of a 31 cm diameter
277 methanol pool fire, similar to the flame in the present work (i.e. a turbulent Reynolds number
278 from 100 to 200). Their results show the ratio of Taylor to Kolmogorov time scales is around
279 2.5:1 at the central core of the fire and 8:1 at the edges of the fire. (For comparison, the ratio of
280 Taylor to Kolmogorov length scales in an isothermal, fully developed, plane, momentum-
281 dominated jet is on the order of 70 [28].) This leads to an estimated Kolmogorov length scale
282 ranging from around 10 mm to 0.4 mm and a time scale ranging from 0.005 to 0.008 s, for the
283 current 15 kW ethylene flame at $2.5D$ in height. In this study, the spatial distance between the
284 thermocouple beads is around 0.5 mm and the time constant for the thinner thermocouple is
285 around 0.015 s, which are comparable with the estimated Kolmogorov length scales. This
286 analysis, however, is still a rough estimation. Further velocity measurements are needed for a
287 detailed discussion.

288

289 4.2 Flame centerline temperature

290 Fig. 5(a) shows the mean, rms and ratio between rms and mean temperatures, i.e. the coefficient
 291 of variation (CV), along the centerline of the flame. The mean temperature reaches a maximum
 292 value at a height of $1.5D$, followed by a slight decrease until $2.5D$, after which the mean
 293 temperature drops due to the end of the flame region; similar results have been reported in the
 294 literature [16,29]. The rms temperature fluctuations show a different trend, which increases from
 295 a height of $1.0D$ with a maximum value at $2.5D$. The CV, $T_{g,rms}/T_{g,mean}$, follows a similar trend
 296 with the rms temperature, but with a maximum value at a height of $3.0D$.

297 Probability density function (PDF) profiles of temperature are presented as a function of height
 298 in Fig. 5(b). At a height of $1.0D$, the temperature PDF shows a single peak distribution with a
 299 temperature value around 1100 K at the maximum probability and a reduced temperature
 300 probability under 600 K . This occurs because, at a height of $1.0D$, a narrow necking region is
 301 present between intermittent ‘puffs’ of the flame, as shown in Fig. 5(c), where the flame is less
 302 turbulent and relatively steady. Insufficient mixing of fuel and air results in less frequency of
 303 flame occurrence, and thus a lower mean and rms temperature. As height increases, buoyancy-
 304 driven turbulence gradually increases, enhancing mixing between fuel and air. Lower
 305 temperatures from 300 K to 600 K are evident in PDF profiles at heights of $1.5D$ to $2.5D$,
 306 meanwhile, PDF profiles shift toward larger values and temperatures higher than 2000 K are
 307 detected. This broader temperature distribution leads to a higher rms temperature. At a height of
 308 $3.0D$, the PDF profile shows a bi-modal distribution, with the upper temperature limits shifting
 309 back to a lower value. This is attributed to the combination of fuel burn out and increased air
 310 entrainment in this region. For larger heights of $3.5D$, the flame is more intermittent and hot
 311 burnt gases and air dominate. The PDF profile again shows a single peak distribution with a
 312 much lower peak temperature.



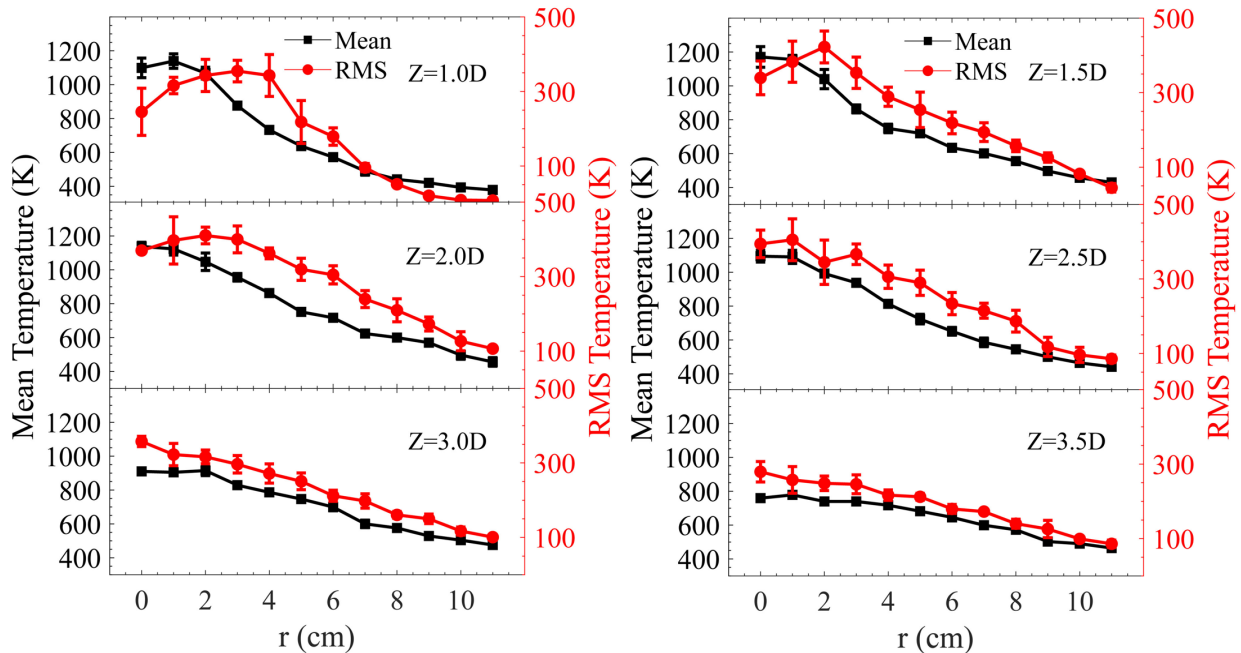
313

314 Fig. 5. Flame centerline temperatures at different heights: (a) mean, rms and ratio of rms and
 315 mean temperatures, (b) PDF profiles of temperature, (c) image of the flame. Note the necking of
 316 the flame at the base which is responsible for significant mixing and variability at the base.

317

318 4.3 Overall temperature statistics

319 To have a better understanding of the overall flame structure, the mean and rms temperature
320 distributions in a two-dimensional plane across the flame centerline were measured, as shown in
321 Fig. 6, where the error bar represents the standard deviation between 2 to 3 repeated
322 measurements. For a height of $1.0D$, a dip in the mean temperature at the flame centerline ($r = 0$
323 ~ 1 cm) is consistently observed. This same trend was also observed by Weckman et al. [16] for
324 methanol pool fires. As discussed before, fuel-rich conditions at this location lead to lower mean
325 and rms temperatures. Away from the centerline, enhanced mixing between fuel and air results in
326 increased mean and rms temperatures. From $1.5D$ to $3.5D$, the mean temperature monotonically
327 decreases moving away from the centerline in the radial direction, with the peak mean
328 temperature near 1200 K. The peak rms temperature fluctuates around $400 \sim 425$ K and is
329 observed 4 cm away from the centerline at $1.0D$. This is consistent with the necking behavior
330 shown in Fig. 5(c), where intense mixing occurs in this region away from the flame centerline.
331 As the height increases, the location of the peak rms temperature moves toward the centerline of
332 the flame. After a height of $2.5D$, the peak rms temperature is located at the flame centerline.



333

334 Fig. 6. Mean and rms temperatures at different heights and radial locations

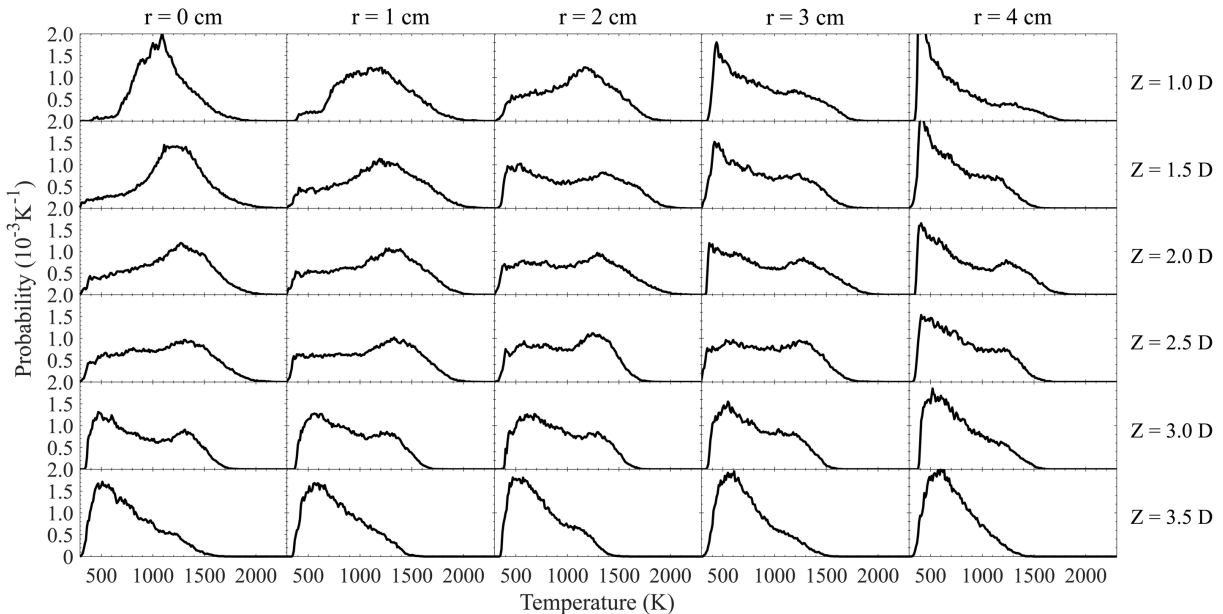
335

336 Temperature PDF profiles in both horizontal (0 to 4 cm) and vertical directions are plotted in
337 Fig. 7. At a height of $1.0D$, there is a large probability of high temperatures, i.e. >1200 K, at
338 $r = 2$ cm, showing good mixing between fuel and air; inward from this location, the
339 environment tends to be fuel rich. For the outward direction, the PDF shifts to a lower value due
340 to increased penetration of ambient air. PDF profiles at a height of $1.5D$ have a similar trend with

341 those at $1.0D$, except the probability of air entrainment into the centerline region increases,
 342 promoting better mixing compared to the $1.0D$ location. From heights of $2.0D$ to $3.5D$, PDF
 343 profiles become similar in the radial direction. A relatively homogeneous region is observed and
 344 enlarged from $0 \sim 2$ cm at a height of $2.0D$ to $0 \sim 4$ cm at $3.0D$. The maximum temperature
 345 decreases from near 2050 K to 1700 K. After a height of $3.0D$, fuel burn out leads to a narrower
 346 temperature range and finally results in single peak distribution at $3.5D$ mainly corresponding to
 347 burnt gas. The probability at high temperatures (i.e. $2000 \sim 2050$ K) is relatively low, around
 348 $5.0E-5$ K^{-1} from $1.0D$ to $2.5D$ near the flame centerline. As a comparison, Kearney et al [4]
 349 measured the temperature profile of a 2-m diameter turbulent pool fire with a 10%-toluene/90%-
 350 methanol fuel using the CARS technique. Their results show that at heights of 0.5 to 1.5 m, the
 351 temperature probability at $2000 \sim 2050$ K has a value ranging from $2E-4$ to $4E-4$. The
 352 discrepancy on the high temperature probability might be attributed to the different fuels and fire
 353 sizes used in these two works. A possible explanation for this low probability at higher
 354 temperatures is that a large amount of air entrainment leads to a sparse presence of the flame
 355 sheet in this turbulent flame.

356

357 Overall, starting from $1.0D$ at the flame centerline, mixing between fuel and air is enhanced both
 358 horizontally and vertically with a corresponding increase in probability of high temperatures, e.g.
 359 the presence of the flame. At the base of the flame, large vortical structures form which oscillate
 360 within the necking flame region. As the flame evolves upward, flow instability increases, and
 361 vortex structures break down into smaller vortices, promoting mixing between fuel and air and
 362 leading to increased mean gas temperatures. Further upward, the combined effects of buoyancy-
 363 induced turbulence development and fuel burnout result in homogeneous burning with a reduced
 364 mean temperature.



365

366

Fig. 7. Temperature probability distribution at different locations

367

368 **5. Conclusions**

369 A dual-thermocouple technique has been applied to a carefully-instrumented turbulent ethylene
370 diffusion flame in order to provide accurate gas temperature measurements. Both sensitivity and
371 uncertainty analyses show that this improved dual-TC technique has advantages under hostile
372 flame environments where the bead diameter may change due to soot deposition or other effects.
373 Measured temperatures were compensated using a temporally-varying time constant, producing a
374 systematic temperature validation dataset for 15 kW buoyant turbulent ethylene flames useful for
375 future model development and validation. The resultant mean, rms and PDF temperature profiles
376 provide a detailed picture of the turbulent flame structure.

377 These temperature measurements, alongside existing data such as the radiant power distribution,
378 local soot volume fraction and soot temperature, as well as future gas velocity measurements will
379 provide a detailed dataset of this flame for validation and development of radiation models. This
380 data is still limited to the 15 kW ethylene diffusion flame investigated. Future applications of the
381 dual-thermocouple technique on different fuels and fire sizes, i.e. a soot-free flame and a larger
382 fire, are needed to improve our understanding of turbulent buoyant flames.

383

384 **Acknowledgements**

385 The authors would like to acknowledge financial support for this work from FM Global and the
386 National Science Foundation through CBET award 1554026 and the INTERN program. The
387 authors would also like to thank Robert Tabinowski, Aaron Cunha and Gennadiy Geyyer of FM
388 Global for their efforts in conducting the experiments.

389

390 **Appendix A.**

391 **Radiant heat flux estimation**

392 The heat flux to a thermocouple bead can be estimated by assuming the thermocouple bead has a
393 diameter of d_i , $i = 1,2$. The fire is idealized to have a cylindrical shape, with a height of
394 $z_f = 0.7$ m, and diameter of $d_f = 0.152$ m. The radiative power per unit volume of the fire
395 (kW/m^3) is

$$396 \quad \dot{q}_r''' = \frac{Q}{V_f} \chi_r, \quad (\text{A.1})$$

397 where Q is the theoretical heat-release rate (15 kW), V_f is the flame volume ($z_f \pi d_f^2 / 4$), and χ_r is
398 the radiant fraction (0.34 for ethylene).

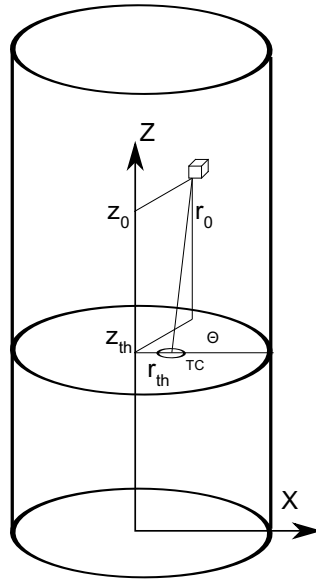
399 Fig. A.1 shows a thermocouple placed at a radius of r_{th} and a height of Z_{th} . For an infinitely-
400 small flame volume element at a height of z_0 , radius of r_0 from the centerline, and an azimuthal
401 angle of θ degree from x axis, the distance of the element to thermocouple is

402
$$d_{th-f} = \{[(r_{th} + r_0) \sin(\theta/2)]^2 + [(r_{th} - r_0) \cos(\theta/2)]^2 + (z_0 - z_{th})^2\}^{1/2}. \quad (A.2)$$

403 The radiant heat flux per unit area to the surface of the thermocouple is

404
$$q''_{r,u} = \int_0^{d_f/2} \int_0^{z_f} \int_0^{2\pi} \frac{r_0 \dot{q}''_r}{4\pi d_{th-f}^2} d\theta dz_0 dr_0. \quad (A.3)$$

405 Using Eq. A.3, \dot{q}''_{rad} for a thermocouple can be determined. The highest possible heat flux is
 406 determined at the center location (0 cm radius, $2.5D=0.38$ m height), with $\dot{q}''_{rad} = 45$ kW/m².



407

408 Fig. A.1 Idealized flame radiant heat flux calculation.

409

410 **6. References**

411 [1] FM Global, FireFOAM, Available from: <http://www.fmglobal.com/modeling>

412 [2] Y. Wang, P. Chatterjee, J.L. De Ris, Large eddy simulation of fire plumes, Proc. Combust.
 413 Inst. 33 (2011) 2473–2480. doi:10.1016/j.proci.2010.07.031.

414 [3] K. McGrattan, S. Hostikka, R. McDermott, J. Floyd, M. Vanella, Fire Dynamics
 415 Simulator User’s Guide, NIST Spec. Publ. 1019 Sixth Ed. (2019) 347. doi:
 416 10.6028/NIST.SP.1019.

417 [4] S.P. Kearney, T.W. Grasser, Laser-diagnostic mapping of temperature and soot statistics
 418 in a 2-m diameter turbulent pool fire, Combust. Flame. 186 (2017) 32–44.
 419 doi:10.1016/j.combustflame.2017.07.018.

420 [5] Z. Wang, W.C. Tam, K.Y. Lee, A. Hamins, Temperature Field Measurements using Thin
 421 Filament Pyrometry in a Medium-Scale Methanol Pool Fire - NIST Technical Note 2031,
 422 (2018). doi:10.6028/NIST.TN.2031.

423 [6] S.B. Hariharan, E.T. Sluder, M.J. Gollner, E.S. Oran, Thermal structure of the blue whirl,
 424 Proc. Combust. Inst. 37 (2019) 4285–4293. doi:10.1016/j.proci.2018.05.115.

- 425 [7] S.B. Hariharan, P.M. Anderson, H. Xiao, M.J. Gollner, E.S. Oran, The blue whirl:
426 Boundary layer effects, temperature and OH* measurements, *Combust. Flame.* 203 (2019)
427 352–361. doi:10.1016/j.combustflame.2019.02.018.
- 428 [8] D. Zeng, P. Chatterjee, Y. Wang, The effect of oxygen depletion on soot and thermal
429 radiation in buoyant turbulent diffusion flames, *Proc. Combust. Inst.* 37 (2019) 825–832.
430 doi:10.1016/j.proci.2018.05.139.
- 431 [9] G. Cox, R. Chitty, A study of the deterministic properties of unbounded fire plumes,
432 *Combust. Flame.* 39 (1980) 191–209. doi:10.1016/0010-2180(80)90016-4.
- 433 [10] O. Korobeinichev, M. Gonchikzhapov, A. Tereshchenko, I. Gerasimov, A. Shmakov, A.
434 Paletsky, A. Karpov, An experimental study of horizontal flame spread over PMMA
435 surface in still air, *Combust. Flame.* 188 (2018) 388–398.
436 doi:10.1016/j.combustflame.2017.10.008.
- 437 [11] S. Brohez, C. Delvosalle, G. Marlair, A two-thermocouples probe for radiation corrections
438 of measured temperatures in compartment fires, *Fire Saf. J.* 39 (2004) 399–411.
439 doi:10.1016/j.firesaf.2004.03.002.
- 440 [12] W.C. Strahle, M. Muthukrishnan, Thermocouple time constant measurement by cross
441 power spectra, *AIAA J.* (1976). doi:10.2514/3.7268.
- 442 [13] M. Vachon, P. Cambray, T. Maciaszek, J.C. Bellet, Temperature and velocity fluctuation
443 measurements in a diffusion flame with large buoyancy effects, *Combust. Sci. Technol.* 48
444 (1986) 223–240. doi:10.1080/00102208608923894.
- 445 [14] S.J. Fischer, B. Hardouin-Duparc, W.L. Grosshandler, The structure and radiation of an
446 ethanol pool fire, *Combust. Flame.* 70 (1987) 291–306. doi:10.1016/0010-2180(87)90110-
447 6.
- 448 [15] M. Kunugi, H. Jinno, Measurements of fluctuating flame temperature, *Symp. (Int.)*
449 *Combust.* 7 (1958) 942–948. doi:10.1016/S0082-0784(58)80141-1.
- 450 [16] E.J. Weckman, A.B. Strong, Experimental investigation of the turbulence structure of
451 medium-scale methanol pool fires, *Combust. Flame.* 105 (1996) 245–266.
452 doi:10.1016/0010-2180(95)00103-4.
- 453 [17] A. Ballantyne, J.B. Moss, Fine wire thermocouple measurements of fluctuating
454 temperature, *Combust. Sci. Technol.* 17 (1977): 63-72. doi:10.1080/00102209708946813.
- 455 [18] L.J. Forney, G.C. Fralick, Two-wire thermocouple: Frequency response in constant flow,
456 *Rev. Sci. Instrum.* 66 (1995) 3331–3336. doi:10.1063/1.1145503.
- 457 [19] P.G. O'Reilly, R.J. Kee, R. Fleck, P.T. McEntee, Two-wire thermocouples: A nonlinear
458 state estimation approach to temperature reconstruction, *Rev. Sci. Instrum.* 72 (2001)
459 3449–3457. doi:10.1063/1.1384428.
- 460 [20] M. Tagawa, Y. Ohta, Two-thermocouple probe for fluctuating temperature measurement
461 in combustion - Rational estimation of mean and fluctuating time constants, *Combust.*
462 *Flame.* 109 (1997) 549–560. doi:10.1016/S0010-2180(97)00044-8.

- 463 [21] P.A. Santoni, T. Marcelli, E. Leoni, Measurement of fluctuating temperatures in a
464 continuous flame spreading across a fuel bed using a double thermocouple probe,
465 Combust. Flame. 131 (2002) 47–58. doi:10.1016/S0010-2180(02)00391-7.
- 466 [22] B. Merci, A. Trouvé, Call for participation in the second workshop organized by the
467 IAFSS Working Group on, Fire Saf. J. 105 (2020) 92–94.
468 doi:10.1016/j.firesaf.2019.02.010.
- 469 [23] A. Brown, M. Bruns, M. Gollner, J. Hewson, G. Maragkos, A. Marshall, R. McDermott,
470 B. Merci, T. Rogaume, S. Stolarov, J. Torero, A. Trouvé, Y. Wang, E. Weckman,
471 Proceedings of the first workshop organized by the IAFSS Working Group on
472 Measurement and Computation of Fire Phenomena (MaCFP), Fire Saf. J. 101 (2018) 1–
473 17. doi:10.1016/j.firesaf.2018.08.009.
- 474 [24] M.C. Croarkin, W.F. Guthrie, G.W. Burns, M. Kaeser, G.F. Strouse, Temperature-
475 Electromotive Force Reference Functions and Tables for the Letter-Designated
476 Thermocouple Types Based on the ITS-90, Natl. Inst. Stand. Technol. Monogr. 175.
477 (1993).
- 478 [25] C.R. Shaddix, Correcting Thermocouple Measurements for Radiation Loss: A Critical
479 Review, Proceedings of the 33rd National Heat Transfer Conference, Albuquerque, New
480 Mexico, August 15–17, 1999.
- 481 [26] B.N. Taylor, C.E. Kuyatt, Guidelines for evaluating and expressing the uncertainty of
482 NIST measurement results, NIST Technical Note 1297, National Institute of Standards
483 and Technology, Gaithersburg, 1994.
- 484 [27] V. Gururajan, F.N. Egolfopoulos, Direct sensitivity analysis for ignition delay times,
485 Combust. Flame. 209 (2019) 478–480. doi:10.1016/j.combustflame.2019.08.007.
- 486 [28] E. Gutmark, I. Wygnanski, The planar turbulent jet, J. Fluid Mech. 73 (1976) 465–495.
487 doi:10.1017/S0022112076001468.
- 488 [29] B.J. McCaffrey, Purely buoyant diffusion flames: some experimental results, NBSIR 79-
489 1910, 1979. doi:NBSIR 79-1910.
- 490